2023

Universal Upper End of the Stellar Initial Mass Function in the Young and Compact LEGUS Clusters

Dooseok Escher Jung

Daniela Calzetti

Matteo Messa

Mark Heyer

Mattia Sirressi

See next page for additional authors

Authors

Dooseok Escher Jung, Daniela Calzetti, Matteo Messa, Mark Heyer, Mattia Sirressi, Sean T. Linden, and et. al.

Universal Upper End of the Stellar Initial Mass Function in the Young and Compact LEGUS Clusters

Dooseok Escher Jung[1], Daniela Calzetti[1], Matteo Messa[2], Mark Heyer[1], Mattia Sirressi[3], Sean T. Linden[1], Angela Adamo[3], Rupali Chandar[4], Michele Cignoni[5], David O. Cook[6], Clare L. Dobbs[7], Bruce G. Elmegreen[8], Aaron S. Evans[9], Michele Fumagalli[10,11], John S. Gallagher, III[12], Deidre A. Hunter[13], Kelsey E. Johnson[9], Robert C. Kennicutt, Jr.[14,15,16], Mark R. Krumholz[17], Daniel Schaerer[18,19], Elena Sabbi[20], Linda J. Smith[20], Monica Tosi[21], and Aida Wofford[22]

[1] Department of Astronomy, University of Massachusetts Amherst, 710 North Pleasant Street, Amherst, MA 01003, USA; djung@umass.edu
[2] Observatoire de Genève, Université de Genève, 51 Ch. des Maillettes, CH-1290 Versoix, Switzerland
[3] Department of Astronomy, Oscar Klein Centre, Stockholm University, AlbaNova, SE-106 91 Stockholm, Sweden
[4] Ritter Astrophysical Research Center, University of Toledo, Toledo, OH 43606, USA
[5] Department of Physics, University of Pisa, Largo Pontecorvo, 3, I-56127 Pisa, Italy
[6] Caltech/IPAC, 1200 E. California Boulevard, Pasadena, CA 91125, USA
[7] School of Physics and Astronomy, University of Exeter, Stocker Road, Exeter EX4 4QL, UK
[8] IBM T.J. Watson Research Center, 1101 Kitchawan Road, Yorktown Heights, NY 10598, USA
[9] Department of Astronomy, University of Virginia, 530 McCormick Road, Charlottesville, VA 22904, USA
[10] Dipartimento di Fisica G. Occhialini, Università degli Studi di Milano-Bicocca, Piazza della Scienza 3, I-20126 Milano, Italy
[11] INAF—Osservatorio Astronomico di Trieste, via G.B. Tiepolo 11, I-34143 Trieste, Italy
[12] Department of Astronomy, University of Wisconsin, 475 N. Charter Street, Madison, WI 53706, USA
[13] Lowell Observatory, 1400 West Mars Hill Road, Flagstaff, AZ 86001, USA
[14] Department of Astronomy and Steward Observatory, University of Arizona, Tucson, AZ 85721, USA
[15] Department of Physics and Astronomy, Texas A&M University, College Station, TX 77843, USA
[16] Institute of Astronomy, University of Cambridge, Madingley Road, Cambridge CB3 0HA, UK
[17] Research School of Astronomy and Astrophysics, Australian National University, Canberra ACT 2601, Australia
[18] Observatoire de Genève, Université de Genève, Chemin Pegasi 51, 1290 Versoix, Switzerland
[19] CNRS, IRAP, 14 Avenue E. Belin, F-31400 Toulouse, France
[20] Space Telescope Science Institute, 3700 San Martin Drive, Baltimore, MD 21218, USA
[21] INAF—OAS Osservatorio di Astrofisica e Scienza dello Spazio, I-40129 Bologna, Italy
[22] Instituto de Astronomia, Universidad Nacional Autonoma de Mexico, Unidad Académica en Ensenada, 22860 Ensenada, Mexico

Abstract

We investigate the variation in the upper end of the stellar initial mass function (uIMF) in 375 young and compact star clusters in five nearby galaxies within ∼5 Mpc. All the young stellar clusters (YSCs) in the sample have ages ≲ 4 Myr and masses above 500 $M_\odot$, according to standard stellar models. The YSC catalogs were produced from Hubble Space Telescope images obtained as part of the Legacy ExtraGalactic UV Survey (LEGUS) Hubble treasury program. They are used here to test whether the uIMF is universal or changes as a function of the cluster's stellar mass. We perform this test by measuring the Hα luminosity of the star clusters as a proxy for their ionizing photon rate, and charting its trend as a function of cluster mass. Large cluster numbers allow us to mitigate the stochastic sampling of the uIMF. The advantage of our approach relative to previous similar attempts is the use of cluster catalogs that have been selected independently of the presence of Hα emission, thus removing a potential sample bias. We find that the uIMF, as traced by the Hα emission, shows no dependence on cluster mass, suggesting that the maximum stellar mass that can be produced in star clusters is universal, in agreement with previous findings.

Unified Astronomy Thesaurus concepts: Star clusters (1567); Young star clusters (1833); Massive stars (732); OB stars (1141); Star formation (1569); Initial mass function (796); Interstellar line emission (844)

1. Introduction

The stellar initial mass function (IMF) is a valuable tool that enables the derivation of physical quantities such as star formation rates (SFRs; Kennicutt 1998) and star formation histories (Tolstoy et al. 2009) from calibrations of light emission. Similarly, the assumed IMF affects theoretical predictions of chemical evolution models on galactic scales (Romano et al. 2005) and stellar feedback into the interstellar/circumgalactic media (Krumholz et al. 2019). To use this tool effectively, it is imperative to establish whether the functional form of the stellar IMF is universal or varies with local or global environments.

Salpeter (1955) was the first to introduce the concept of the stellar IMF, the mass distribution of stars at birth, as a single power law with a slope $\Gamma \sim 1.35$ in the mass range ~ 3–$15\,M_\odot$, in the form:

$$\Phi(\log m) = \frac{dN}{d \log m} \propto m^{-\Gamma}, \qquad (1)$$

where $\log m$ is the logarithmic mass of the star and N is the number of stars between $\log m$ and $\log m + d \log m$.

Miller & Scalo (1979) found that the slope is shallower at masses lower than those examined by Salpeter (1955), and fitted the IMF with both a segmented power law and a log-normal

function. Kroupa ([2001](#)) revised the multisegmented power law to have $\Gamma = -0.7$ for substellar objects ($M < 0.08\,M_\odot$), $\Gamma = 0.3$ in the lower stellar mass regime (0.08–$0.5\,M_\odot$), and $\Gamma = 1.3$ for stars with $M > 0.5\,M_\odot$. Chabrier ([2003](#)) also fitted the IMF with a log-normal function:

$$\phi(m) \sim \exp\left(-\frac{\log m - \log m_c}{2\sigma^2}\right), \qquad (2)$$

where m_c is the characteristic mass and σ is the dispersion of the log-normal distribution. The Chabrier-type IMF is almost indistinguishable from the Kroupa-type IMF (Dabringhausen et al. [2008](#)). In the context of this paper, therefore, the IMF is termed "universal" if its shape, slopes in the case of the functional form in Kroupa ([2001](#)), and upper/lower stellar limits are independent of the local or global environment.

The debate on whether or not the IMF depends on other parameters, such as metallicity, environmental properties, etc., has been ongoing for several decades. Some authors argue that the stellar IMF is universal (Massey [2003](#); Bastian et al. [2010](#); Oey [2011](#); Weisz et al. [2012](#)), while other studies find nonuniversal IMFs, with variations that are dependent on the galactic environment (Fardal et al. [2007](#); Wilkins et al. [2008](#); Van Dokkum & Conroy [2011](#); Cappellari et al. [2012](#); Kroupa et al. [2012](#); Geha et al. [2013](#)). For example, using star counts, Schneider et al. ([2018](#)) found that the slope of the high-mass IMF in 30 Doradus, a giant H II region in the Large Magellanic Cloud, is shallower than the Salpeter/Kroupa value. Counting stars is generally considered the most accurate method to derive the IMF.

However, counting stars individually is challenging, especially when studying potential IMF variations in the massive-star regime due to the evolution of stars and star clusters. The most massive stars are short lived ($\lesssim 3$ Myr) and their numbers are significantly lower than those of low-mass stars. Moreover, they are mainly found in the dense environments of star clusters, where crowding becomes an issue (Kalari et al. [2022](#)). The mass segregation that occurs in gravitationally bound systems makes more massive stars sink toward the center of the stellar clusters over time, and causes low-mass stars to be dynamically ejected. As a result, in the crowded areas of the cluster centers, massive stars are difficult to distinguish individually, and low-mass stars can remain undetected due to their faintness or because of ejection from the cluster itself (Maíz-Apellániz [2008](#); Ascenso et al. [2009](#)). Thus, the problem of crowding complicates attempts at resolving high-mass stars even with the angular resolution of the Hubble Space Telescope (HST). The proximity of the Magellanic Clouds (distances ~ 50–60 kpc) has helped overcome some of these complications and stars heavier than $\sim 150\,M_\odot$ have been found in the core of R136, the central cluster in 30 Doradus (Crowther et al. [2010](#); Brands et al. [2022](#); Kalari et al. [2022](#)). By using semiresolved star clusters of intermediate masses ($10^3\,M_\odot$–$10^4\,M_\odot$) in M31 (~ 1 Mpc), Weisz et al. ([2015](#)) found that the slope of the high-mass IMF ($\gtrsim 2$–$3\,M_\odot$) in the clusters is close to the Kroupa value ($\Gamma = 1.45^{+0.03}_{-0.06}$) for the same stellar mass range.

An alternative method to individual star counting consists of measuring the integrated or summed IMF of a young stellar population. This method avoids the issues of the resolved-star approach; however, it comes with challenges of its own. Ideally, the population needs to be very young ($\lesssim 3$ Myr, to contain massive stars), coeval (to provide one representation of

the IMF), and homogeneous (to sample the same IMF across the population). Young star clusters (YSCs) provide, at least in principle, such a population. The challenges consist in (1) deriving accurate masses and ages for the star clusters, and (2) deriving the IMF in an unambiguous way from the integrated light of the young cluster population. The latter is challenging even for massive stars, which tend to dominate the light output of YSCs. Furthermore, an accurate census of massive stars can be hindered by feedback, which causes high infant mortality rates in stellar clusters; less than 20% of cluster systems survive longer than 10 Myr (Lada & Lada [2003](#)). A dispersed cluster becomes difficult to recognize as a single-age entity for the purpose of measuring the IMF.

Dispersed clusters contribute their stars to the field and produce an integrated mass function, sometimes called the present-day mass function (PDMF; Miller & Scalo [1979](#)). Because high-mass stars disappear before the low-mass stars have scattered away from their birthplace in the galaxy, the PDMF in any limited region has a complicated relationship to the IMF, and they are not equivalent. Also, if the SFR increases with time, then the summed mass function for all the remaining stars will be shallower than the original cluster's IMF (Elmegreen & Scalo [2006](#)). Even for a steady SFR, and accounting for all the stars that ever formed in, e.g., a young, presupernova region, the summed IMF from many clusters is not necessarily the same as the IMFs of the individual clusters. They are the same only if the stellar mass is randomly sampled from a universal IMF with a power-law shape to infinitely high mass, or if the cluster mass function (CMF) has a slope equal to -2 or shallower (Elmegreen [2006](#)).

If the maximum mass of the star(s) depends physically on the cluster mass, increasing with cluster or molecular cloud mass for example (Larson [1982](#); Kroupa & Weidner [2003](#)) and not just randomly due to the size-of-sample effect (Elmegreen [1983](#)), then the summed IMF can be steeper than the individual IMF. This is because a lot of clusters sum together to yield low-mass stars but only the highest-mass clusters sum together to yield the high-mass stars. To get purely stochastic sampling (a randomly sampled population of massive stars that can occur in clusters with mass $< 10^5\,M_\odot$, i.e., with too low a mass to sample the IMF fully) with a summed IMF slope equal to the individual cluster's slope, some low-mass clusters have to produce high-mass stars. Because cluster-forming cloud complexes are usually much more massive than individual stars, there is typically enough gas to do this. Available observations of the Milky Way bulge, large star fields, and whole galaxies confirm that the summed IMF from composite star-forming regions is about equal to the IMF from individual star-forming regions (Elmegreen [2006](#)).

Pflamm-Altenburg et al. ([2009](#)) considered the implications of a physical, rather than stochastic, relation between the mass of the the most massive star (m_{max}) and the mass of the embedded cluster (M_{ecl}) that hosts the star(s) with m_{max}, generally expressed as the m_{max}–M_{ecl} relation. Embedded clusters are those clusters that are still retaining their original gas, and are therefore about twice as massive as their exposed counterparts, which we term YSCs (Kroupa & Boily [2002](#)). Pflamm-Altenburg et al. ([2009](#)) developed models for an integrated galactic initial mass function (IGIMF) to test the m_{max}–M_{ecl} relation on galactic scales. They found that this relation can explain observations such as the systematic dearth of Hα emission in low-mass galaxies, if low-mass, low-density

galaxies mostly form low-mass clusters which, in turn, form a smaller number of massive stars than expected from a fully sampled IMF. Weidner et al. (2010) summarized several theoretical studies that predict the m_{max}–M_{ecl} relation. In addition, they reported several observational results that show that m_{max} and M_{ecl} are correlated in resolved stars and clusters, suggesting that the m_{max}–M_{ecl} relation has general validity. Oey (2011) further extended this concept to explain the steepness of the Salpeter IMF in star clusters as the result of an initial clump mass function with a slope of -2 combined with the inability of low-mass clumps to form massive stars. Similar considerations can be used to explain the steeper H II region luminosity function in the interarm regions relative to the spiral arms of galaxies (Oey & Clarke 1998). Yan et al. (2017) found that the IGIMF model explains well the correlation between SFR and the mass of the most massive star cluster ($M_{ecl, max}$) in the host galaxy, and produce a prediction for the expected supernova rate in very-low-SFR galaxies. Jeřábková et al. (2018) applied the IGIMF framework to calculate grids of models that depend on both metallicity and SFR. Their IGIMF model can potentially explain several observational results, including the evolution of the time-varying IMF in massive elliptical galaxies.

Conversely, Fumagalli et al. (2011), suggested that the IGIMF cannot fully describe the observed large scatter in the Hα/far-ultraviolet (FUV) ratio for low-luminosity galaxies regardless of their SFR. After adding stochasticity and time evolution to a Kroupa (2001) IMF and convolving the IMF with the CMF, Fumagalli et al. (2011) reproduced the observed $L_{H\alpha}/L_{FUV}$ ratios of dwarf galaxies without the need to implement the IGIMF framework. Similar results were obtained by Hermanowicz et al. (2013) for the $L_{H\alpha}/L_{FUV}$ ratios of a large sample of H II regions extracted from eight nearby star-forming galaxies.

In an attempt to discriminate among these different results, Calzetti et al. (2010) used the integrated light from the YSC population to test the universality of the upper end of the stellar initial mass function (uIMF), bypassing the traditional method of individual star counts. Based on Corbelli et al. (2009), individual YSCs were divided in bins of stellar mass and the properties of the clusters were combined together within each mass bin to emulate a high-mass cluster. One of the combined properties is the luminosity of the hydrogen recombination-line intensity, Hα, as a tracer of the ionizing photon rate, which is a proxy for the number of massive and ionizing stars present in the star clusters located within H II regions (Oey & Clarke 1998). This method allows one to investigate the universality of the uIMF in star clusters across a wide range of masses, including those below $\sim3000\,M_\odot$, which are subject to significant stochastic sampling (Cervino et al. 2002). The application of this method to the cluster populations in the nearby galaxies NGC 5194, NGC 4214, and M83 (Calzetti et al. 2010; Andrews et al. 2013, 2014) shows that the clusters with even the lowest mass down to $500\,M_\odot$ produce high-mass stars up to $120\,M_\odot$. Thus, according to these authors, the maximal star mass is not dependent on the mass of its parent cluster, implying disagreement with a physically based m_{max}–M_{ecl} relation (Weidner et al. 2010).

Intriguingly, Weidner et al. (2014) argued that, in the case of NGC 4214, the addition of stochastic sampling helps reconcile the trends observed in the cluster population of this galaxy with the m_{max}–M_{ecl} relation, opposite to the conclusions of Andrews

et al. (2013). However, NGC 4214 alone is not a good test sample for the m_{max}–M_{ecl} relation due to its relatively low SFR ($0.2\,M_\odot\,yr^{-1}$), which implies low numbers of observed clusters, and thus, low-number statistics.

Progress on this controversy can be aided by the data products from the Legacy ExtraGalactic UV Survey (LEGUS), a Hubble treasury program that has obtained imaging data for ~50 nearby star-forming galaxies (distances ~ 3.5–18 Mpc) in five bands from near-ultraviolet (NUV) to I (Calzetti et al. 2015b). As part of the effort, star cluster catalogs for 31 LEGUS galaxies have been produced, which include visual identification, location, and photometry for each star cluster; for clusters detected in more than four bands, physical parameters such as age, mass, and color excess, $E(B-V)$, derived from spectral energy distribution (SED) fitting (Adamo et al. 2017), are included as well.

The LEGUS collaboration has already investigated the general properties of the YSC populations in the observed galaxies, including the CMF and cluster luminosity functions (CLFs). Adamo et al. (2017), Messa et al. (2018b), and Cook et al. (2019) generalized the -2 slope power-law behavior of the CMFs and CLFs to a much larger sample of galaxies than previously analyzed including dwarf galaxies. Adamo et al. (2017) and Messa et al. (2018a, 2018b) determined the value of the upper mass truncation to the CMF, and investigated its dependency on galactic environment. Adamo et al. (2017) also showed that the different evolutionary timescales between YSCs and compact associations track the hierarchical process of star formation (Grasha et al. 2015, 2017a, 2017b). The investigation of the spatial correlation between the LEGUS YSCs and molecular clouds in M51 and NGC 7793 showed that the younger the clusters, the closer they tend to be located to the molecular clouds, spiral arms, and the galactic center (Grasha et al. 2018, 2019). Orozco-Duarte et al. (2022) developed a photometric library of synthetic star clusters with stochastically sampled IMFs; by comparing their models with the YSCs in NGC 7793 from the LEGUS catalogs, those authors determined that the physical quantities (ages, masses, and extinctions) are highly model dependent and most clusters have multipeaked age probability distributions.

The present study builds on the results of earlier studies, with the goal of testing whether or not the uIMF varies as a function of the stellar mass of YSCs, using the large cluster catalogs of the LEGUS collaboration (Calzetti et al. 2015b; Adamo et al. 2017). We combine the star clusters from the catalogs of selected LEGUS galaxies with archival Hα imaging data to repeat the analysis of Andrews et al. (2013, 2014). Our approach differs from those papers in that the clusters are selected independently of whether they have detected line emission or not. In this way, we do not bias our analysis, since we do not exclude low-mass clusters that may be missing massive, ionizing stars due to stochastic sampling. Section 2 explains the data collection and the image processing. Section 3 describes how we use our data to get to a description of the uIMF. In Section 4, we discuss our results and their implications.

2. Data

LEGUS is an HST Treasury Program (Cycle 21) which collected five band images (UV, U, B, V, and I) of 50 star-forming galaxies within 12 Mpc with the Wide-Field Camera 3 (WFC3) using the filters F275W, F336W, F438W, F555W, and

Table 1
Properties of the LEGUS Galaxies in This Study

Name[a]	R.A.[a]	Decl.[a]	Morph.[a]	Dist.[b] (Mpc)	$M_\star$[b] ($M_\odot$)	$E(B-V)$[a]	Z[c]	SFR (UV)[b] ($M_\odot$ yr^{-1})
NGC 1313	03:18:30.05	−66:28:45.0	SBd	4.39	2.6×10^9	0.0965	0.008	1.15
NGC 1705	04:54:13.7	−53:21:40.9	SA0/BCG	5.1	1.3×10^8	0.0071	0.008	0.11
NGC 4395	12:25:56.60	33:31:10.1	SAm	4.3	6.0×10^8	0.0152	0.004	0.34
NGC 4449	12:28:12.06	44:05:42.3	IBm	4.31	1.1×10^9	0.0171	0.004	0.94
NGC 7793	23:57:40.86	−32:35:20.6	SAd	3.44	3.2×10^9	0.0171	0.008	0.52

Notes.
[a] Galaxy name, coordinates (J2000), morphological type, and the foreground color excess (A_V/R_V) due to the dust in our Milky Way, as listed in the NASA Extragalactic Database (NED).
[b] Distance, stellar mass, and SFR of each galaxy from Calzetti et al. (2015b).
[c] Metallicity of each galaxy, from Sabbi et al. (2018).

F814W (Calzetti et al. 2015b). Archival images obtained with the Advanced Camera for Surveys (ACS) wide field in the filters F435W, F606W, and F814W are also used when they are available to complement the LEGUS observations. The pixel scale of ACS/WFC is slightly larger, 0″.05 pixel^{-1}, than that of WFC3 (0″.0396 pixel^{-1}), but the LEGUS collaboration aligned and resampled the images to the WFC3 ones.

YSC catalogs were produced using a combination of SExtractor (Bertin & Arnouts 1996) for the automatic search of extended sources and human identification. SED fits for all sources detected with a signal-to-noise ratio of 3 or better in at least four bands were performed, and the sources were assigned ages, masses, and extinctions with uncertainties. The YSC catalogs are complete out to ∼200 Myr in age and down to masses between 500 and 5000 $M_\odot$, depending on the age of the source. Details on the catalog production and characteristics can be found in Adamo et al. (2017). We supplement the LEGUS observations with archival images in the WFC3/F657N or ACS/F658N and the adjacent WFC3/F547M or ACS/F550M (as available) filters to measure the hydrogen recombination line (Hα).

2.1. Galaxy and Cluster Selection

As our goal is to measure the ionizing photon rate of each YSC, we need to separate the ionization regions of neighboring YSCs from each other. This sets an upper limit of about 5 Mpc to the maximum distance of the galaxies whose YSC-produced ionization regions we can resolve with HST. Within this distance limit, individual clusters can be detected down to ∼500 $M_\odot$ (Andrews et al. 2014), which allows our study to investigate whether massive stars are able to be formed in low-mass clusters. We also require that the YSCs exhibit a low dust color excess, $E(B-V) < 0.1$ mag, to avoid heavy impact from extinction corrections. This choice is likely to select against the youngest (most embedded) YSCs, but it also enables accurate accounting of the ionizing photon rate. The clusters in the LEGUS catalogs show on average low extinction values, typically $E(B-V) \lesssim 0.2$ mag (Adamo et al. 2017; Messa et al. 2018b). After applying these selection criteria, our sample includes five nearby star-forming galaxies with distances ≲ 5 Mpc. The galaxies span an order of magnitude in SFRs (0.1–1.2 $M_\odot$ yr^{-1}) and stellar masses (10^8–10^9 $M_\odot$); these and other global properties are listed in Table 1.

The cluster candidates in the LEGUS catalogs have been classified according to four morphological classes as defined in Adamo et al. (2017). Class 1 candidates are symmetric and concentrated. Class 2 candidates look less symmetric and rather

Table 2
Statistics of the LEGUS Star Clusters by Class and by Galaxy for Ages within 1–4 Myr, $E(B-V) \leqslant 0.2$, and Mass Over 500 $M_\odot$ Used in This Study

Name	Class 1	Class 2	Class 3	Total (Each Galaxy)
NGC 1313	27	51	88	166
NGC 1705	0	1	1	2
NGC 4395	20	42	53	115
NGC 4449	6	5	2	13
NGC 7793	15	34	30	79
Total	68	133	174	375

elongated relative to class 1. Class 3 candidates are asymmetric, less compact, and have multiple peaks joined by diffuse emission in between the peaks. Candidates in both class 1 and class 2 are considered YSCs while class 3 candidates are "compact associations." Class 4 candidates are "nonclusters:" artifacts, background galaxies, single stars, or asterisms. In our analysis, we only use the candidates of classes 1, 2, and 3 as real star clusters; class 4 sources will not be considered any further.

Since we are trying to characterize the uIMF, we require our YSCs to have undergone minimal evolution. We choose clusters with ages ⩽ 4 Myr and treat them as coeval objects that have not yet undergone supernova events or strong gas expulsion (Weidner et al. 2010; Relaño et al. 2012). Leakage of ionizing photons from H II regions can still occur, and can affect our results, as we discuss below. We require cluster masses above 500 $M_\odot$. This ensures that our YSCs are not dominated by misclassified single massive stars (Andrews et al. 2014), but are still probing stochastic sampling effects. After all selections are applied, we have 375 clusters in total for this study (Table 2). Figure 1 shows the locations of the clusters identified as class 1, 2, and 3 in NGC 4449.

2.2. Photometry

In order to measure the Hα luminosity of each star cluster, we retrieve from the Hubble Legacy Archive images of the five galaxies in the F547M/F550M (V-short) and in the F657N/F658N (Hα+[N II]) filters obtained with WFC3/ACS. We give preference for the medium-band F550M or F547M over the F555W filter to avoid the strong [O III] emission line which affects the broader filter. We align the images to the F814W (I band) images of the LEGUS data for aperture photometry and additional corrections. Aperture photometry is performed on all 375 clusters in all three bands using the PHOTUTILS package in ASTROPY with a 5 pixel aperture radius,
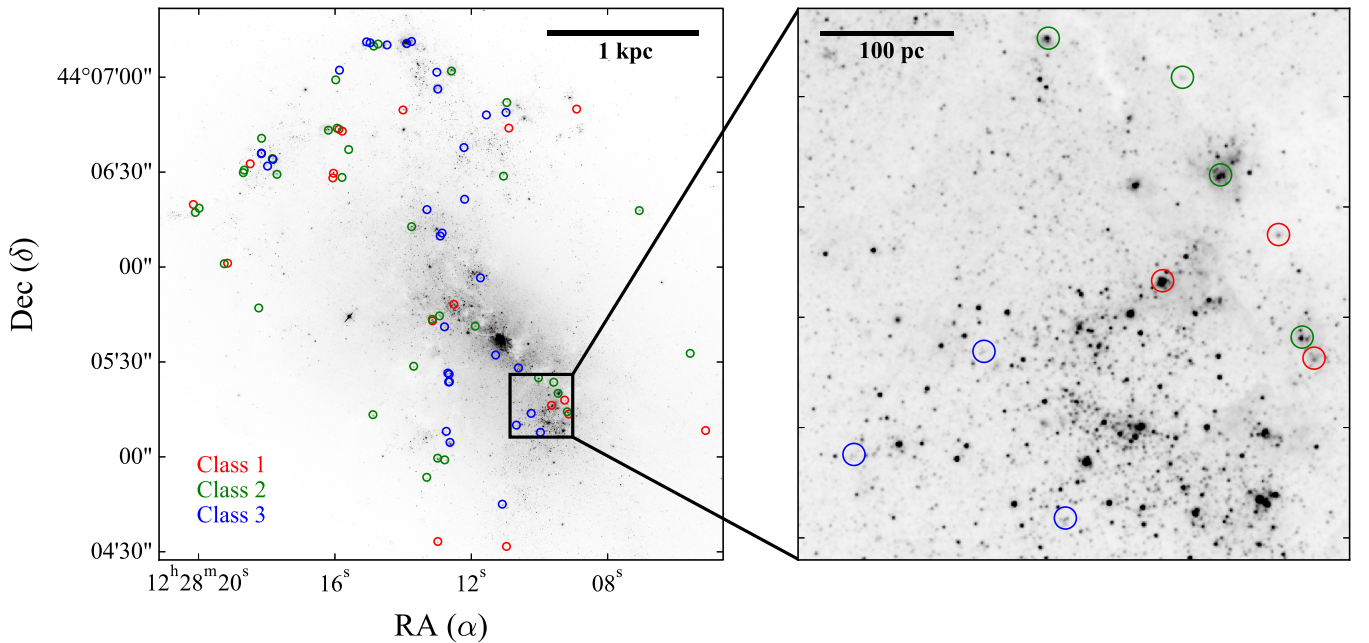
Figure 1. Left: the locations of the selected LEGUS clusters by class (class 1 as red, class 2 as green, and class 3 as blue circles) with ages within 1–4 Myr in NGC 4449 are shown in the F555W image. Right: a zoomed-in image of the selected area (the black solid square) in the left panel. Candidates identified as class 4 are excluded here and the morphology-based cluster classification is explained in Section 2.1.

corresponding to 0.35–0.5 $R_{\text{Strömgren}}$ (Calzetti et al. 2010), and with an annulus between a 7 and 9 pixel radius for the local background. The positions of the selected clusters are taken from the LEGUS catalogs.

The flux density in each band is obtained by converting counts to erg cm^{-2} s^{-1} after local background subtraction. Flux densities of Hα in each cluster are measured from the difference between the observed flux density in the Hα +[N II] filters (F657N/F658N) and that of the underlying stellar continuum in the narrow-band image obtained from the interpolation between the F547M/F550M and the F814W filters. The flux conversion keyword PHOTFLAM from the images' header is then used to convert the counts to physical units. Finally, we convert the flux densities to fluxes in Hα +[N II] by multiplying our measurements by the FWHMs of the narrow-band filters. In the case of undetected Hα, the detection limits of each cluster in the F657N/F658N filters are reported as upper limits.

Aperture corrections are applied to all photometry measurements. Continuum-subtracted Hα+[N II] (F657N/F658N) images were used to select isolated sources with strong emission to construct curves of growth. The final aperture correction is derived from the average calculated for isolated sources. The typical correction is a factor of ∼2.3. As our sources are all extremely young, the nebular emission, when present, is generally concentrated and coincident with the location of the star cluster's stellar emission. Thus, we do not find large variations in the correction factor. Removal of the contamination by [N II] in the (F657N/F658N) filters is performed by applying the average ratios of [N II] to Hα of each galaxy to the flux densities in Hα+[N II] (Kennicutt et al. 2008).

Extinction correction for $L_{\text{H}\alpha}$ is performed considering two contributions: the foreground Milky Way color excess, $E(B-V)_{\text{MilkyWay}}$, and the color excess intrinsic to the cluster, $E(B-V)_{\text{cluster}}$. The latter is determined from SED fitting

of the cluster's photometry (Adamo et al. 2017). For the intrinsic attenuation of the nebular gas, we adopt the recipe of Calzetti et al. (1994, 2000), who established $E(B-V)_{\text{gas}} = E(B-V)_{\text{cluster}}/0.44$. The attenuation affecting the star cluster can then be expressed as:

$$F_{\text{int}}(\lambda) = F_{\text{obs}}(\lambda) \, 10^{\,0.4\,E(B-V)\,k(\lambda)} \qquad (3)$$

where $k(\lambda) = 2.54$ for Hα and $E(B-V) = E(B-V)_{\text{Milky Way}} + E(B-V)_{\text{cluster}}/0.44$. Figure 2 shows an example of the spatial distribution of the selected clusters for this study in NGC 4449, indicating whether the Hα emission is present or absent, and assigning color coding to their ages and masses.

3. Analysis and Results

The number of massive stars in a cluster can be inferred from the hydrogen ionizing photon rate, $Q(\text{H}^0)$, due to the strong ionizing emission from young and hot OB stars. The Hα luminosity, $L_{\text{H}\alpha}$, of a cluster is a tracer of $Q(\text{H}^0)$, such that we can test whether or not the uIMF depends on cluster mass by normalizing $L_{\text{H}\alpha}$ by the cluster mass (M_{cl}; Calzetti et al. 2010).

The distributions of the ratio $L_{\text{H}\alpha}/M_{\text{cl}}$ for our cluster samples is shown as histograms of the relative frequencies for individual galaxies and for all samples combined in Figure 3; we plot separately the Hα-detected clusters and the undetected ones as upper limits. The $\log(L_{\text{H}\alpha}/M_{\text{cl}})$ values cover the range 31–35 when all 375 YSCs are considered. The ratio $L_{\text{H}\alpha}/M_{\text{cl}}$ of the selected clusters in the five galaxies are shown individually in Figure 4. We can hardly see any clear trend between $L_{\text{H}\alpha}/M_{\text{cl}}$ and M_{cl}, suggesting a weak correlation between m_{max} and M_{cl}.

The clusters with undetected Hα emission represent 54% of the total number of sources and are located ∼1.8 orders of magnitude on average below the sources with Hα emission. Given that the majority of our star clusters have masses below ∼3000 $M_{\odot}$ (Figure 4), the large number of sources without Hα
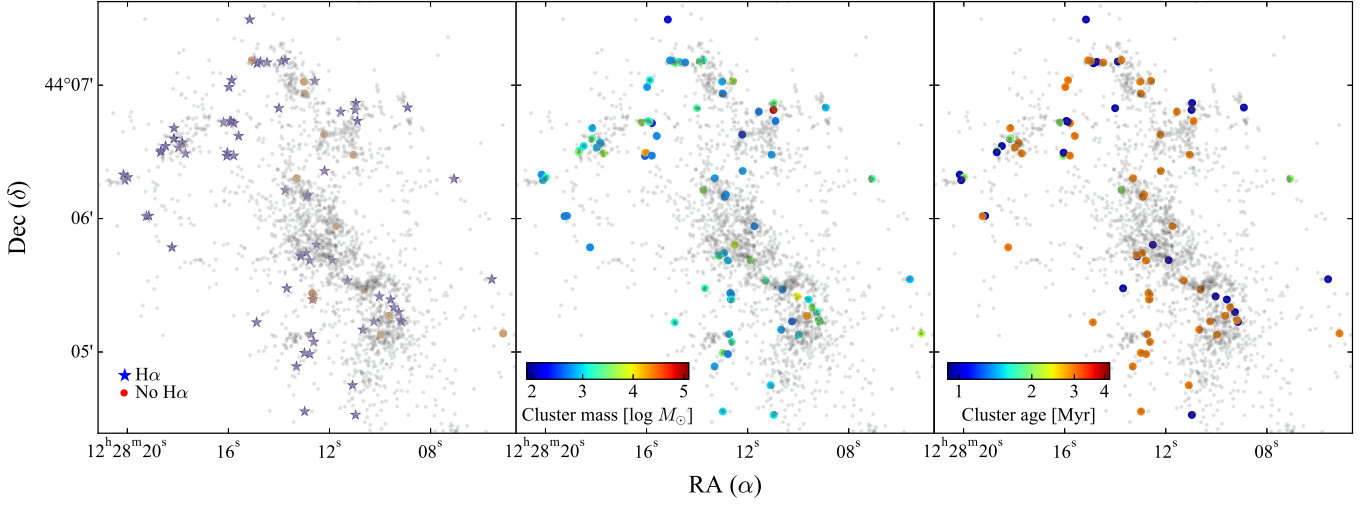
Figure 2. The spatial distribution of the star clusters in NGC 4449 selected for this study, and showing the presence/absence of Hα (left), their masses (middle), and their ages (right). The values of the masses (10^2–$10^5 \, M_\odot$) and the ages (1–4 Myr) are shown by the color bars in the middle and right panels, respectively. The gray dots are all star clusters in NGC 4449 from the LEGUS catalogs.
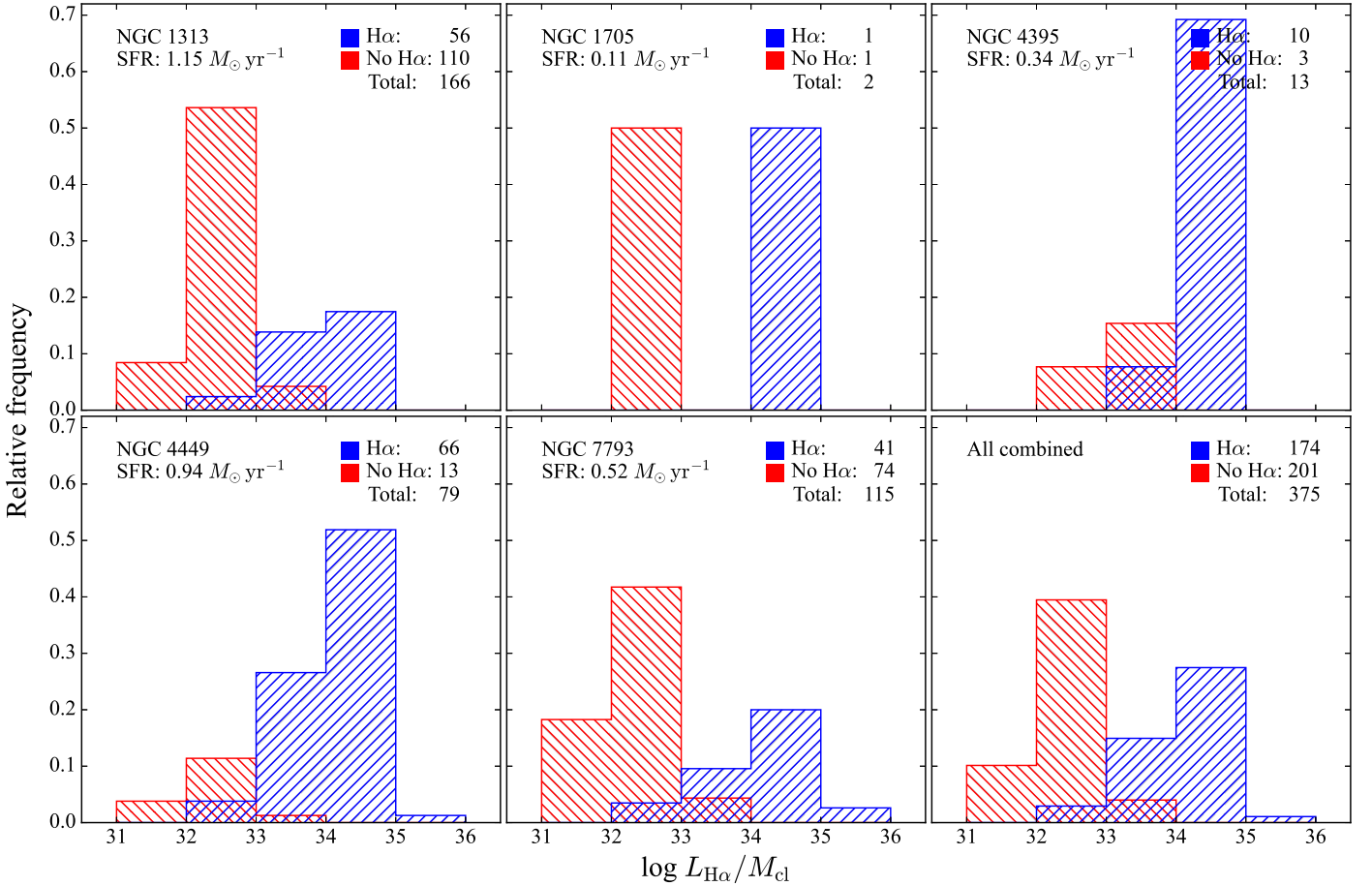

Figure 3. The distribution of $L_{H\alpha}/M_{cl}$ values for each galaxy and for all samples combined. The blue bars are Hα-emission-detected sources and the red bars are undetected ones, for which the indicated values are upper limits. For the sources detected in Hα, the typical two-sided 1σ uncertainties are about 1/2 bin in size. The SFR of each galaxy is given under the name of the galaxies.

emission is easily explainable as an effect of the stochastic sampling of the IMF in this regime. Thus, Figure 3 supports that the LEGUS sample selection is unbiased relative to the presence or absence of nebular emission. The gap between the two distributions is likely an effect of our measurement

technique coupled with evolutionary effects of the clusters. For instance, very young clusters hosting massive stars can develop energetic stellar winds over short timescales that remove the nebular gas surrounding the cluster (MacKenty et al. 2000; Krumholz et al. 2019). Thus, we cannot exclude that, at least
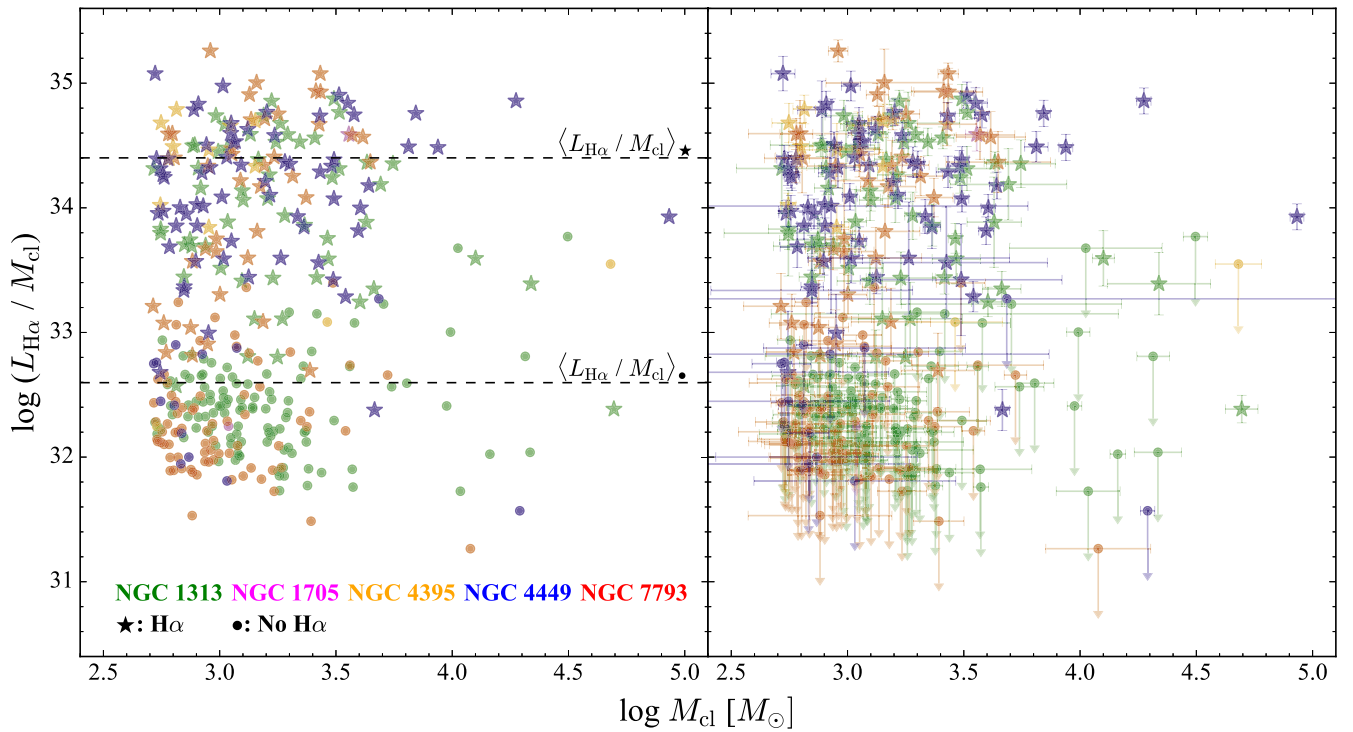
Figure 4. Left: the ratio $L_{H\alpha}/M_{cl}$ of all the selected clusters as a function of stellar mass, as listed in the LEGUS catalogs. Star markers are the clusters with $H\alpha$ emission, and dots are those without $H\alpha$ emission. For the latter, the indicated values of $L_{H\alpha}$ are upper limits. Dashed horizontal lines are the average of $L_{H\alpha}/M_{cl}$ for the sources detected in $H\alpha$ ($\langle L_{H\alpha}/M_{cl}\rangle_\star$) and those undetected in the line ($\langle L_{H\alpha}/M_{cl}\rangle_\bullet$), respectively. Right: the same plot as the left panel, but including the error bars of each cluster. Here the upper limits are clearly marked.

for some of the sources without detected $H\alpha$ emission, the lack of detection is due to purely morphological effects because the $H\alpha$ emission may actually be present but located in a shell around the cluster (MacKenty et al. 2000; Calzetti et al. 2010, 2015a; Relaño et al. 2012; Andrews et al. 2013; Belfiore et al. 2022). An extreme example is the case of young, UV-bright starbursts with high SFRs and many massive O stars but which lack ionized gas due to ionizing photon leakage (Marques-Chaves et al. 2022). In this case, our photometric measurements provide a lower limit to the true nebular emission. We cannot correct for this effect as most of our sources are located in crowded regions, where their $H\alpha$ emission overlaps with that of neighboring sources and shells of nebular emission cannot be easily identified and measured.

Conversely, we expect many of the low-mass sources undetected in $H\alpha$ to be subject to stochastic sampling effects, meaning that their low masses prevent them from forming massive stars in significant numbers. In these cases, the sources cannot ionize the surrounding gas and our reported $H\alpha$ values are upper limits. As we cannot discriminate, for the $H\alpha$-undetected sources, between the upper limits from stochastic sampling and the lower limits from expelled gas (see above), we will consider both cases in the analysis that follows.

Before binning by mass to mitigate stochasticity, we check whether the physical parameter we use, the cluster mass, may be influenced by the way the SED fitting is performed on the photometry of the clusters in the LEGUS catalogs (Adamo et al. 2017). In other words, we want to make sure that the values of the cluster masses are not biased by potential covariances in the SED fitting results due to photometric uncertainties. In order to perform this assessment, we carry out the same procedure as in Figure 4 but using purely observational quantities, i.e., the I-band (F814W) flux

density instead of M_{cl}. The choice of this band is driven by its low sensitivity to extinction. Figure 5 shows the distribution of the clusters' $L_{H\alpha}/L_I$ as a function of L_I. Figure 5 has, in the low-luminosity regime ($L_I < 38$), a comparable scatter to Figure 4 in the low-mass regime; there is a gap between the averages of $L_{H\alpha}/L_I$ for sources detected and undetected in $H\alpha$, of comparable magnitude to the gap in Figure 4. The errors in $L_{H\alpha}/L_I$ do not show a trend as a function of L_I, again similar to the data in Figure 4. This suggests that the clusters' $L_{H\alpha}$ and their masses are not strongly correlated with each other, and there is no bias in using the cluster mass as our reference parameter.

We test the $m_{max}-M_{ecl}$ relation with the approach suggested by Calzetti et al. (2010). The IMF and the IGIMF are equivalent under the assumption of a universal IMF. The only effect at play is stochastic sampling, which is predominant at low cluster masses (Hermanowicz et al. 2013). A low-mass cluster will be missing stars at randomly sampled masses; since, for a typical IMF functional shape, there are far more low-mass stars than high-mass stars, random sampling will affect the latter more than the former. In order to be truly stochastic, the incomplete sampling needs to be erased when accumulating multiple low-mass clusters together. That is, the shape of the IMF resulting from the sum of 100 individual clusters each with a mass of $1000\,M_\odot$ will be equivalent to the IMF of a single $10^5\,M_\odot$ cluster (Elmegreen 2000, 2006; Bastian et al. 2010; Calzetti et al. 2010). So, we sum all of the values of $L_{H\alpha}/M_{cl}$ as:

$$\left\langle \frac{L_{H\alpha}}{M_{cl}} \right\rangle = \frac{\Sigma_i\, L_{H\alpha,i}}{\Sigma_i\, M_{cl,i}}, \qquad (4)$$

which we divide into several mass bins of equal total mass (Table 3) to test any trend of the uIMF with mass
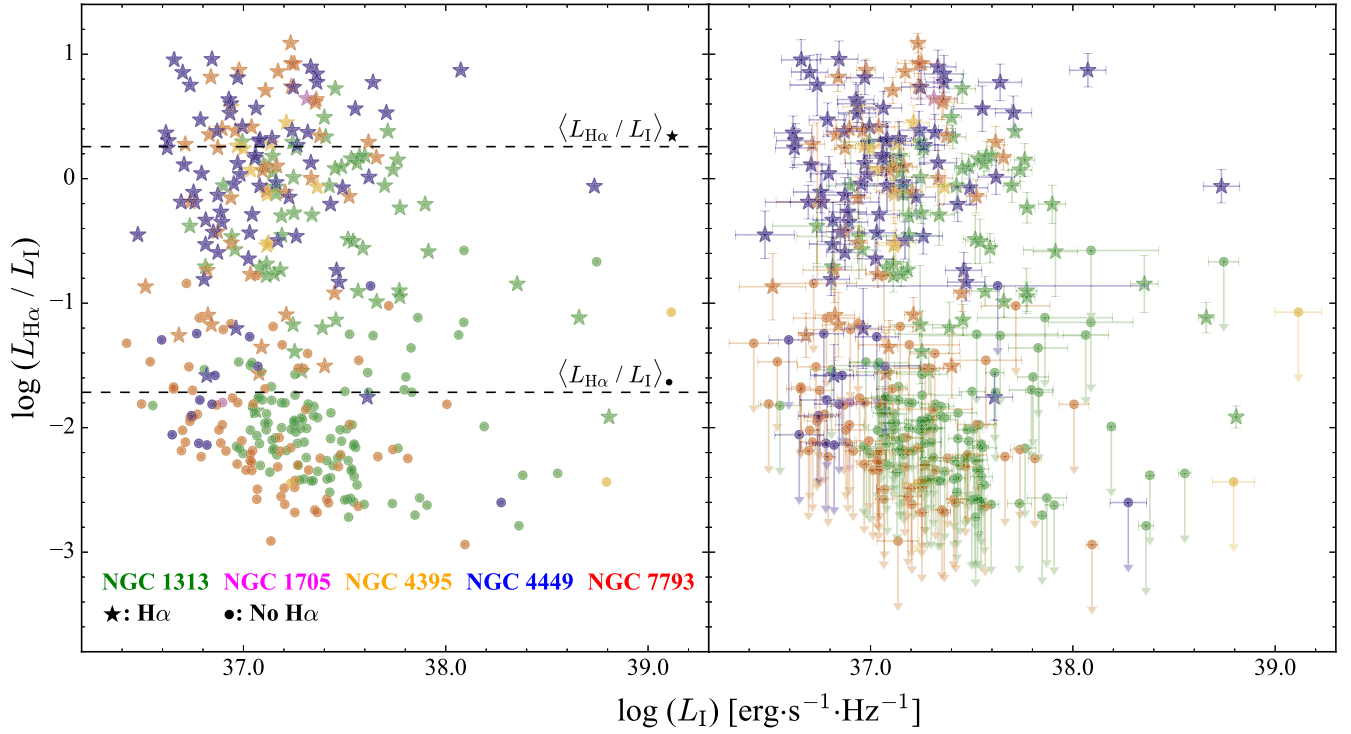
Figure 5. The ratio $L_{H\alpha}/L_I$ of the cluster samples in this study as a function of L_I. This figure has the same structure as Figure 4 but for L_I instead of M_{cl}.

Table 3
Statistics on the Binned Data by Mass in Each Individual Galaxy and in All Galaxies Combined

Name and Bin No.	$\langle M \rangle$ ($M_\odot$)	Mass Range ($M_\odot$)	No. of Clusters	M_{total} ($M_\odot$)	$\langle L_{H\alpha}/M_{cl} \rangle$	$\sigma_{\langle L_{H\alpha}/M_{cl} \rangle}$[a]
NGC 1313						
Bin 1	1.235×10^3	$5.211 \times 10^2 - 2.348 \times 10^3$	127	1.569×10^5	33.819	0.0256
Bin 2	4.685×10^3	$2.358 \times 10^3 - 1.260 \times 10^4$	33	1.546×10^5	33.876	0.0687
Bin 3	2.658×10^4	$1.452 \times 10^4 - 4.957 \times 10^4$	6	1.595×10^5	33.224	0.237
NGC 1705						
Bin 1	2.342×10^3	$1.091 \times 10^3 - 3.592 \times 10^3$	2	4.683×10^3	33.475	0.131
NGC 4395						
Bin 1	8.448×10^2	$5.366 \times 10^2 - 1.422 \times 10^3$	11	9.292×10^3	34.500	0.0486
Bin 2	2.544×10^4	$2.902 \times 10^3 - 4.797 \times 10^4$	2	5.087×10^4	33.532	0.488
NGC 4449						
Bin 1	1.193×10^3	$5.205 \times 10^2 - 3.102 \times 10^3$	64	7.637×10^4	34.292	0.0388
Bin 2	5.911×10^3	$3.259 \times 10^3 - 1.881 \times 10^4$	13	7.685×10^4	34.604	0.480
Bin 3	5.260×10^4	$1.952 \times 10^4 - 8.567 \times 10^4$	2	1.052×10^5	33.839	0.103
NGC 7793						
Bin 1	7.684×10^2	$5.172 \times 10^2 - 1.181 \times 10^3$	69	5.302×10^4	33.834	0.0489
Bin 2	1.643×10^3	$1.193 \times 10^3 - 2.445 \times 10^3$	33	5.422×10^4	34.123	0.0397
Bin 3	4.067×10^3	$2.471 \times 10^3 - 1.197 \times 10^4$	13	5.287×10^4	34.396	0.0745
All galaxies						
Bin 1	1.087×10^3	$5.172 \times 10^2 - 2.317 \times 10^3$	293	3.186×10^5	34.038	0.0160
Bin 2	4.368×10^3	$2.348 \times 10^3 - 1.452 \times 10^4$	73	3.189×10^5	34.176	0.119
Bin 3	3.522×10^4	$1.881 \times 10^4 - 8.567 \times 10^4$	9	3.170×10^5	33.900	0.0786

Note.
[a] Propagated in $\log_{10}$ scale.

(Andrews et al. 2013, 2014). We include in the sum above also clusters that are undetected in $H\alpha$ to avoid biasing our results (Weidner et al. 2014).

Figure 6 shows the $\langle L_{H\alpha}/M_{cl} \rangle$ values in bins of cluster mass, for each galaxy and for the entire sample combined. The data

are divided into several mass bins to check the $m_{max}-M_{ecl}$ relation except for NGC 1705, which has only one data point located at $M_{cl} \sim 10^{3.4} M_\odot$ due to the small cluster catalog (only two YSCs, Table 2). The value of the maximum mass bin in NGC 7793 is ~ 10 times lower than those of the other galaxies,
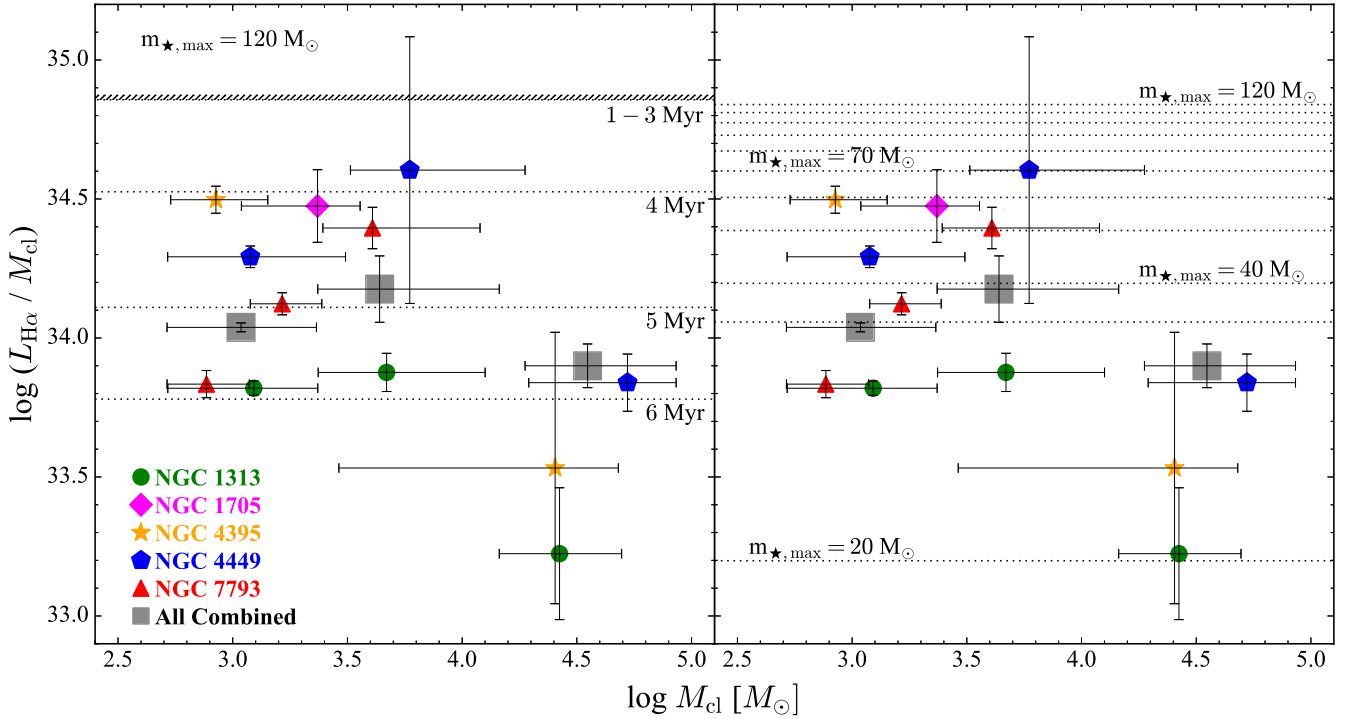
Figure 6. Left: the location of $\langle L_{H\alpha}/M_{cl}\rangle$ ($=\Sigma L_{H\alpha}/\Sigma M_{cl}$) with their standard deviations (Table 3) as a function of the mean of the sample's mass in each bin. Different colors and shapes identify different galaxies. The dark-gray squares are the $\langle L_{H\alpha}/M_{cl}\rangle$ ratios of all galaxies combined, as a function of binned mass. The horizontal bar associated with each symbol shows the size of each mass bin. The horizontal dotted lines show the evolution of model $\langle L_{H\alpha}/M_{cl}\rangle$ as a function of age (1–6 Myr) with fixed $m_{max} = 120\ M_\odot$ from SB99. Right: the same data points as in the left panel shown with a range of model upper mass values m_{max} averaged within the 1–4 Myr age produced by SB99 from 20 $M_\odot$ to 120 $M_\odot$ in 10 $M_\odot$ intervals (horizontal dotted lines).

so $\langle L_{H\alpha}/M_{cl}\rangle$ of NGC 7793 does not cover the higher-mass range ($M_{cl} \gtrsim 10^{3.5}\ M_\odot$) of the YSCs covered by the other four galaxies.

In order to compare the observational uIMFs to theoretical ones, we generate models using STARBURST99 (SB99; Leitherer et al. 1999) with a standard Kroupa IMF up to $m_{max} = 120\ M_\odot$, Padova stellar evolution tracks with AGB stars, and metallicity $Z = 0.004$. The choice of metallicity for the models is consistent with the metallicity of the sample galaxies (Table 1). The data points in Figure 6 are compared with cluster models with both fixed m_{max} but different ages (left panel) and different m_{max} averaged over the age range 1–4 Myr (right panel). After distributing the clusters into three mass bins, the total equivalent masses in each bin are $3.186 \times 10^5\ M_\odot$, $3.189 \times 10^5\ M_\odot$, and $3.170 \times 10^5\ M_\odot$ for the mass bins centered at $1.087 \times 10^3\ M_\odot$, $4.368 \times 10^3\ M_\odot$, and $3.522 \times 10^4\ M_\odot$, respectively. The mass range of each bin is $5.172 \times 10^2\ M_\odot$–$2.317 \times 10^3\ M_\odot$, $2.348 \times 10^3\ M_\odot$–$1.452 \times 10^4\ M_\odot$, and $1.881 \times 10^4\ M_\odot$–$8.567 \times 10^4\ M_\odot$, respectively. More details on the binned data for each galaxy and for the combined sample are given in Table 3. To test the impact of upper limits on our binned values, we replace all upper limits with zero luminosity in Hα ($L_{H\alpha} = 0$). We find that that impact is negligible due to the small contribution ($\lesssim 1.6\%$) of the upper limits to the mean value of $L_{H\alpha}/M_{cl}$ in Equation (4) (Figure 4).

The distribution of $\langle L_{H\alpha}/M_{cl}\rangle$ for the combined sample shows a plateau as a function of mass rather than following the increasing trend for increasing mass described by the m_{max}–M_{ecl} relation (Weidner et al. 2010). Taking $\langle L_{H\alpha}/M_{cl}\rangle \sim 10^{34}$ erg s^{-1} $M_\odot^{-1}$ as our fiducial value at high cluster masses, the expected value at $M_{cl} = 10^3\ M_\odot$ ($M_{ecl} \sim 2 \times 10^3\ M_\odot$) should be about 0.5 dex lower according to the IGIMF models. We do not observe such a decrease, which is several standard deviations below our fiducial

value at that mass (Figure 6). Furthermore, the $\langle L_{H\alpha}/M_{cl}\rangle$ values in the highest-mass bins, $M_{cl} \sim 10^{4.5}\ M_\odot$, are lower than those at lower mass, similarly to what observed in NGC 4214 (Andrews et al. 2013).

The most likely reason for this decrease is that massive star clusters statistically host massive stars more frequently than lower-mass clusters, implying that feedback from those massive stars can effectively expel gas from the cluster location, an effect magnified in clusters residing in low H I density regions (Pellegrini et al. 2012). Gas expulsion implies that there is less gas nearby to produce Hα. This is observed in the most massive cluster in NGC 4214, where the presence of P Cygni profiles for UV lines like Si IV ($\lambda \sim 1400$ Å) and C IV ($\lambda \sim 1550$ Å) indicates young ages, ~ 4 Myr (Leitherer et al. 1996, 2002), but the cluster occupies a cavity in ionized gas (MacKenty et al. 2000).

The horizontal dotted lines in the left panel (Figure 6) show the theoretical $L_{H\alpha}/M_{cl}$ as a function of cluster age. We expand the range of ages to 6 Myr, which is broader than in our sample selection, because we include the uncertainties in the age determinations of the clusters, estimated to be 1–2 Myr (Adamo et al. 2017). There is almost no difference in the theoretical values of the ratios among 1–3 Myr located at $L_{H\alpha}/M_{cl} \sim 34.8$. $L_{H\alpha}/M_{cl}$ becomes lower when the age of the cluster increases to 6 Myr ($L_{H\alpha}/M_{cl} \sim 33.7$). Nearly all data points are above $L_{H\alpha}/M_{cl}$ at 6 Myr except those of the highest-mass bins in NGC 1313 and NGC 4395 where most of the sources undetected in Hα are located in shell-like or diffused H II regions, possibly due to massive stellar feedback.

The right panel in Figure 6 shows a comparison of the observed $\langle L_{H\alpha}/M_{cl}\rangle$ and the theoretical values of $L_{H\alpha}/M_{cl}$ as a function of m_{max}. The theoretical uIMFs are calculated using

SB99 with different $m_{\max}$ values from $20\,M_\odot$ to $120\,M_\odot$ in $10\,M_\odot$ steps. The Hα luminosities are averaged within the 1–4 Myr age range for each $m_{\max}$ bin. The uIMFs of all data points are distributed below $m_{\max} \sim 70\,M_\odot$ at $m_{\max} \sim 30$–$40\,M_\odot$. As already remarked, this may point to the ages of our sample clusters being somewhat older than our assumed ~ 4 Myr, and consistent with ages as old as ~ 6 Myr.

Although the distribution of $\langle L_{\mathrm{H}\alpha}/M_{\mathrm{cl}}\rangle$ is relatively flat as a function of cluster mass in the mass range ~ 500–$50{,}000\,M_\odot$ (Figure 6), we find that the ionizing photon flux is significantly lower than expected for young ($\lesssim 4$ Myr) star clusters populated with a universal Kroupa IMF (Kroupa 2001) with an upper mass cutoff heavier than $100\,M_\odot$. In other words, the combined sample data (gray squares) are located in correspondence with the $\langle L_{\mathrm{H}\alpha}/M_{\mathrm{cl}}\rangle$ values expected for populations with ages between 5 and 6 Myr. In addition to the uncertainties in the ages, as already discussed above, we consider here ionizing photon leakage out of the star clusters. Although we attempt to recover as much of the $L_{\mathrm{H}\alpha}$ as possible, we cannot measure ionizing photon leakage directly. The escape fraction of ionizing photons from H II regions is estimated to be around 40%–60% by previous studies of diffuse ionized gas in nearby galaxies (Oey et al. 2007; Pellegrini et al. 2012; Belfiore et al. 2022). We have some indirect evidence of this process from the difference in the average $L_{\mathrm{H}\alpha}/M_{\mathrm{cl}}$ values for NGC 1313 and NGC 4449. The average values for the clusters in NGC 4449 are a factor of ~ 5 systematically higher than those of NGC 1313, for all mass bins. NGC 4449 is a higher-density galaxy than NGC 1313; comparing their SFR surface densities as a proxy for gas density, previous studies show $\Sigma_{\mathrm{SFR}} \sim 0.04\,M_\odot\,\mathrm{yr}^{-1}\,\mathrm{kpc}^{-2}$ for NGC 4449 (Annibali et al. 2011) and $\Sigma_{\mathrm{SFR}} \sim 0.01\,M_\odot\,\mathrm{yr}^{-1}\,\mathrm{kpc}^{-2}$ for NGC 1313 (Silva-Villa & Larsen 2011; Messa et al. 2021). Thus, to the extent that lower-density regions are also more porous (Pellegrini et al. 2012), our data support significant ionizing photon leakage out of the H II regions surrounding the star clusters in NGC 1313. This finding is in line with other results, indicating that high-SFR regions, like, e.g., the central starburst in the spiral M83, may be less porous than low-SFR regions and contain clusters that do not tend to leak ionizing photons (Della Bruna et al. 2022).

In the binned mass plot (Figure 6), NGC 7793 is the only galaxy with an obvious trend of increasing $\langle L_{\mathrm{H}\alpha}/M_{\mathrm{cl}}\rangle$ with increasing mass, which may support the $m_{\max}$–M_{ecl} model. However, the other four galaxies do not display a comparable trend, and NGC 7793 does not contain clusters with masses $> 1.2 \times 10^4\,M_\odot$, which leaves any inference about such trends inconclusive. Furthermore, in the lowest-mass bin in NGC 7793, 75% of the clusters have $\lesssim 10^3\,M_{\mathrm{cl}}$ and $L_{\mathrm{H}\alpha}/M_{\mathrm{cl}} < 10^{33.4}$. This characteristic produces a mass bin with a value of $\langle L_{\mathrm{H}\alpha}/M_{\mathrm{cl}}\rangle$ that is much lower for NGC 7793 than for the other galaxies. As a counterpoint, only 23% of the clusters that make NGC 4449's lowest-mass bin have $\lesssim 10^3\,M_{\mathrm{cl}}$, and this flattens considerably the trend of $\langle L_{\mathrm{H}\alpha}/M_{\mathrm{cl}}\rangle$ with cluster mass for this galaxy.

Finally, irrespective of the observed trend, there are numerous low-mass clusters, $\sim 10^3\,M_\odot$ and lower, in all the sample galaxies but NGC 1705, which have significant emission in Hα (Figure 4), even stronger emission than the sources at masses $\gtrsim 5000\,M_\odot$. The presence of Hα-emitting low-mass clusters indicates that stochasticity is a major contributor to the ionized gas emission of star clusters, further supporting our results.

4. Summary and Conclusion

We have investigated the possibility of a nonuniversal uIMF using catalogs of YSCs. Star clusters represent prime targets for this test due to the quasi-single-age nature of their stellar populations.

We choose five nearby galaxies within ~ 5 Mpc with a broad range of SFRs as calculated from dust-corrected UV (0.1–$1.2\,M_\odot\,\mathrm{yr}^{-1}$) LEGUS data (Calzetti et al. 2015b). The cluster catalogs of these galaxies (Adamo et al. 2017) are used to test variations of the uIMF and we limit our analysis to YSCs and compact associations with ages within 1–4 Myr and masses over $500\,M_\odot$ (as determined from SED fits) to mitigate uncertainties due to the evolution of massive stars out of the main sequence in older clusters. We include sources without Hα emission to prevent our results from being affected by biases, due to the stochastic nature of the IMF sampling, which disfavors presence of massive stars in low-mass clusters.

Our analysis includes photometry of the Hα emission in correspondence of all YSCs identified in the five galaxies. The Hα emission is obtained from imaging in the HST Hα+[N II] (F657N or F658N) filters, after stellar continuum subtraction using the interpolated stellar emission between V-short and I, as well as removal of the [N II] contamination in the F657N/ F658N filters. We apply aperture corrections to account for the ionized gas outside of the photometric apertures by using growth curves derived from isolated Hα-emitting sources.

Our results, shown in Figure 6, are consistent with those of Andrews et al. (2013, 2014), in that the mass-normalized ionizing photon flux is basically constant with cluster mass. This implies that the IMF from which the cluster populations are drawn is universal. The $\langle L_{\mathrm{H}\alpha}/M_{\mathrm{cl}}\rangle$ values in Figure 6 do not strongly follow the trend expected in the $m_{\max}$–M_{ecl} relation of Weidner et al. (2010). The three mass bins of the combined clusters are centered at $1 \times 10^3\,M_\odot$, $4.4 \times 10^3\,M_\odot$, and $3.5 \times 10^4\,M_\odot$, shown as gray squares in Figure 6, and their $\langle L_{\mathrm{H}\alpha}/M_{\mathrm{cl}}\rangle$ values mark a relatively constant trend, around ~ 30–$40\,M_\odot$ for the most massive stars. This value can be explained if our sample, which is selected to include clusters up to ~ 4 Myr, actually includes clusters potentially as old as ~ 6 Myr, due to uncertainties in the age determinations, as well as significant ionizing photon leakage out of the H II regions. Leakage can lower the measured Hα luminosity by about a factor of 2, on average (Oey et al. 2007; Pellegrini et al. 2012; Belfiore et al. 2022).

Looking at individual galaxies, only NGC 7793 shows a trend consistent with the $m_{\max}$–M_{ecl} relation (Figure 6). However, this galaxy lacks clusters more massive than $1.2 \times 10^4\,M_\odot$, which leaves the issue unsettled. In addition, several low-mass clusters in NGC 7793, down to $\sim 10^3\,M_\odot$, show significant Hα emission (Figure 4), implying the low-mass clusters host massive stars.

The $\langle L_{\mathrm{H}\alpha}/M_{\mathrm{cl}}\rangle$ values of the heaviest mass bin at $\sim 10^{4.5}\,M_\odot$ are lower than those of the other mass bins both for individual galaxies and for the combined sample. This finding had been reported in Andrews et al. (2013, 2014) and is likely caused by feedback effects from the faster dynamical evolution in higher-mass clusters.

We have confirmed that the uIMF is consistent with a universal trend, and deviations are due to stochasticity, in good agreement with previous studies (Calzetti et al. 2010; Andrews et al. 2013, 2014). More cluster samples, especially from galaxies spanning a larger range of metallicities and SFRs than those explored here, would be desirable to provide a definite

test of the dependence of the maximum mass of stars on the cluster masses where they are embedded.

Furthermore, infrared observations would allow us to obtain a census of the clusters that are still deeply embedded in their natal clouds, and are missing from our accounting. These tend to be the youngest among our clusters, typically with ages $\leqslant 3$ Myr (Messa et al. 2021). These embedded clusters are the most promising for sampling the youngest stars and the unexpanded gas regions they ionize. Future observations with the James Webb Space Telescope are likely to provide such samples of embedded clusters even in more distant galaxies then 5 Mpc, thanks to Webb's better resolution in the infrared than the HST.

Acknowledgments

ORCID iDs

Dooseok Escher Jung ● https://orcid.org/0000-0003-2797-9979
Daniela Calzetti ● https://orcid.org/0000-0002-5189-8004
Matteo Messa ● https://orcid.org/0000-0003-1427-2456
Mark Heyer ● https://orcid.org/0000-0002-3871-010X
Mattia Sirressi ● https://orcid.org/0000-0002-0923-8352
Sean T. Linden ● https://orcid.org/0000-0002-1000-6081
Angela Adamo ● https://orcid.org/0000-0002-8192-8091
Rupali Chandar ● https://orcid.org/0000-0003-0085-4623
Michele Cignoni ● https://orcid.org/0000-0001-6291-6813
David O. Cook ● https://orcid.org/0000-0002-6877-7655
Clare L. Dobbs ● https://orcid.org/0000-0002-4578-297X
Bruce G. Elmegreen ● https://orcid.org/0000-0002-1723-6330
Aaron S. Evans ● https://orcid.org/0000-0003-2638-1334
Michele Fumagalli ● https://orcid.org/0000-0001-6676-3842
John S. Gallagher, III ● https://orcid.org/0000-0001-8608-0408
Deidre A. Hunter ● https://orcid.org/0000-0002-3322-9798
Kelsey E. Johnson ● https://orcid.org/0000-0001-8348-2671
Robert C. Kennicutt, Jr. ● https://orcid.org/0000-0001-5448-1821
Mark R. Krumholz ● https://orcid.org/0000-0003-3893-854X
Daniel Schaerer ● https://orcid.org/0000-0001-7144-7182
Elena Sabbi ● https://orcid.org/0000-0003-2954-7643
Linda J. Smith ● https://orcid.org/0000-0002-0806-168X
Monica Tosi ● https://orcid.org/0000-0002-0986-4759
Aida Wofford ● https://orcid.org/0000-0001-8289-3428

References

Adamo, A., Ryon, J. E., Messa, M., et al. 2017, ApJ, 841, 131
Andrews, J. E., Calzetti, D., Chandar, R., et al. 2013, ApJ, 767, 51
Andrews, J. E., Calzetti, D., Chandar, R., et al. 2014, ApJ, 793, 4
Annibali, F., Tosi, M., Aloisi, A., & Van Der Marel, R. P. 2011, AJ, 142, 129
Ascenso, J., Alves, J., & Lago, M. T. 2009, A&A, 495, 147
Bastian, N., Covey, K. R., & Meyer, M. R. 2010, ARA&A, 48, 339
Belfiore, F., Santoro, F., Groves, B., et al. 2022, A&A, 659, A26
Bertin, E., & Arnouts, S. 1996, A&AS, 117, 393
Brands, S. A., De Koter, A., Bestenlehner, J. M., et al. 2022, A&A, 663, A36
Calzetti, D., Armus, L., Bohlin, R. C., et al. 2000, ApJ, 533, 682
Calzetti, D., Chandar, R., Lee, J. C., et al. 2010, ApJL, 719, 158
Calzetti, D., Johnson, K. E., Adamo, A., et al. 2015a, ApJ, 811, 75
Calzetti, D., Kinney, L. A., & Storchi-Bergmann, T. 1994, ApJ, 429, 582
Calzetti, D., Lee, J. C., Sabbi, E., et al. 2015b, AJ, 149, 51
Cappellari, M., McDermid, R. M., Alatalo, K., et al. 2012, Natur, 484, 485
Cervino, M., Valls-Gabaud, D., Luridiana, V., & Mas-Hesse, J. M. 2002, A&A, 381, 51
Chabrier, G. 2003, PASP, 115, 763
Cook, D. O., Lee, J. C., Adamo, A., et al. 2019, MNRAS, 484, 4897
Corbelli, E., Verley, S., Elmegreen, B. G., & Giovanardi, C. 2009, A&A, 495, 479
Crowther, P. A., Schnurr, O., Hirschi, R., et al. 2010, MNRAS, 408, 731
Della Bruna, L., Adamo, A., Mcleod, A. F., et al. 2022, A&A, 666, A29
Elmegreen, B. G. 1983, MNRAS, 203, 1011
Elmegreen, B. G. 2000, in ESA Spec. Publ. 445, Star Formation from the Small to the Large Scale, ed. F. Favata, A. Kaas, & A. Wilson (Noordwijk: ESA), 265
Elmegreen, B. G. 2006, ApJ, 648, 572
Elmegreen, B. G., & Scalo, J. 2006, ApJ, 636, 149
Fardal, M. A., Katz, N., Weinberg, D. H., & Davé, R. 2007, MNRAS, 379, 985
Fumagalli, M., Da Silva, R. L., & Krumholz, M. R. 2011, ApJL, 741, L26
Geha, M., Brown, T. M., Tumlinson, J., et al. 2013, ApJ, 771, 29
Grasha, K., Calzetti, D., Adamo, A., et al. 2015, ApJ, 815, 93
Grasha, K., Calzetti, D., Adamo, A., et al. 2017a, ApJ, 840, 113
Grasha, K., Calzetti, D., Adamo, A., et al. 2019, MNRAS, 483, 4707
Grasha, K., Calzetti, D., Bittle, L., et al. 2018, MNRAS, 481, 1016
Grasha, K., Elmegreen, B. G., Calzetti, D., et al. 2017b, ApJ, 842, 25
Hermanowicz, M. T., Kennicutt, R. C., & Eldridge, J. J. 2013, MNRAS, 432, 3097
Jeřábková, T., Hasani Zonoozi, A., Kroupa, P., et al. 2018, A&A, 620, 1
Kalari, V. M., Horch, E. P., Salinas, R., et al. 2022, ApJ, 935, 162
Kennicutt, R. C., Jr. 1998, ApJ, 498, 541
Kennicutt, R. C., Jr., Lee, J. C., Funes, J. G., et al. 2008, ApJS, 178, 247
Kroupa, P. 2001, MNRAS, 322, 231
Kroupa, P., & Boily, C. M. 2002, MNRAS, 336, 1188
Kroupa, P., & Weidner, C. 2003, ApJ, 598, 1076
Kroupa, P., Weidner, C., Pflamm-Altenburg, J., et al. 2012, in Planets, Stars and Stellar Systems, ed. T. D. Oswalt & G. Gilmore, Vol. 5 (Berlin: Springer), 115
Krumholz, M. R., McKee, C. F., & Bland-Hawthorn, J. 2019, ARA&A, 57, 227
Lada, C. J., & Lada, E. A. 2003, ARA&A, 41, 57
Larson, R. B. 1982, MNRAS, 200, 159
Leitherer, C., Calzetti, D., & Martins, L. P. 2002, ApJ, 574, 114
Leitherer, C., Schaerer, D., Goldader, J. D., et al. 1999, ApJS, 1, 3
Leitherer, C., Vacca, W. D., Conti, P. S., et al. 1996, ApJ, 465, 717
MacKenty, J. W., Maiz-Apellaniz, J. S., Pickens, C. E., Norman, C. A., & Walborn, N. R. 2000, AJ, 120, 3007
Maíz-Apellniz, J. 2008, ApJ, 677, 1278
Marques-Chaves, R., Schaerer, D., Alvarez-Marquez, J., et al. 2022, MNRAS, 517, 2972
Massey, P. 2003, ARA&A, 41, 15
Messa, M., Adamo, A., Calzetti, D., et al. 2018a, MNRAS, 477, 1683
Messa, M., Adamo, A., Ostlin, G., et al. 2018b, MNRAS, 473, 996
Messa, M., Calzetti, D., Adamo, A., et al. 2021, ApJ, 909, 121
Miller, G. E., & Scalo, J. M. 1979, ApJS, 41, 513
Oey, M. S. 2011, ApJL, 739, L46
Oey, M. S., & Clarke, C. J. 1998, AJ, 115, 1543
Oey, M. S., Meurer, G. R., Yelda, S., et al. 2007, ApJ, 661, 801
Orozco-Duarte, R., Wofford, A., Vidal-García, A., et al. 2022, MNRAS, 509, 522
Pellegrini, E. W., Oey, M. S., Winkler, P. F., et al. 2012, ApJ, 755, 40
Pflamm-Altenburg, J., Weidner, C., & Kroupa, P. 2009, MNRAS, 395, 394
Relaño, M., Kennicutt, R. C., Eldridge, J. J., Lee, J. C., & Verley, S. 2012, MNRAS, 423, 2933
Romano, D., Karakas, A. I., Tosi, M., & Matteucci, F. 2005, A&A, 430, 491
Sabbi, E., Calzetti, D., Ubeda, L., et al. 2018, ApJS, 235, 23
Salpeter, E. E. 1955, ApJ, 121, 161
Schneider, F. R. N., Sana, H., Evans, C. J., et al. 2018, Sci, 361, 69
Silva-Villa, E., & Larsen, S. S. 2011, A&A, 529, A25
The Astropy Collaboration, Price-Whelan, A. M., Lim, P. L., et al. 2022, ApJ, 935, 167
Tolstoy, E., Hill, V., & Tosi, M. 2009, ARA&A, 47, 371
Van Dokkum, P. G., & Conroy, C. 2011, ApJL, 735, L13
Weidner, C., Kroupa, P., & Bonnell, I. A. 2010, MNRAS, 401, 275
Weidner, C., Kroupa, P., & Pflamm-Altenburg, J. 2014, MNRAS, 441, 3348
Weisz, D. R., Johnson, B. D., Johnson, L. C., et al. 2012, ApJ, 744, 44
Weisz, D. R., Johnson, L. C., Foreman-Mackey, D., et al. 2015, ApJ, 806, 198
Wilkins, S. M., Hopkins, A. M., Trentham, N., & Tojeiro, R. 2008, MNRAS, 391, 363
Yan, Z., Jerabkova, T., & Kroupa, P. 2017, A&A, 607, 1